Available online at www.sciencedirect.com

ScienceDirect

Energy Procedia 77 (2015) 215 – 224

Energy Procedia

5th International Conference on Silicon Photovoltaics, SiliconPV 2015

Numerical modeling of c-Si PV modules by coupling the semiconductor with the thermal conduction, convection and radiation equations

Malte R. Vogt[a,*], Hendrik Holst[b], Matthias Winter[a], Rolf Brendel[a,b] and Pietro P. Altermatt[a]

[a]*Dep. Solar Energy, Inst. Solid-State Physics, Leibniz University of Hannover, Appelstr. 2, 30167 Hanover, Germany*
[b]*Institute for Solar Energy Research Hamelin (ISFH), Am Ohrberg 1, 31860 Emmerthal, Germany*

Abstract

Commonly, the thermal behavior of solar cell modules is calculated with analytical approaches using non wavelength-dependent optical data. Here, we employ ray tracing of entire solar modules at wavelengths of 300-2500 nm to calculate heat sources. Subsequently, finite element method (FEM) simulations are used to solve the semiconductor equations coupled with the thermal conduction, thermal convection, and thermal radiation equations. The implemented model is validated with measurements from an outdoor test over the period of an entire year. Our ray tracing analysis of different solar modules under the AM.15G spectrum shows that, for a standard module about 18.9% of the sun's intensity becomes parasitically absorbed. A loss analysis shows that the biggest parasitic heat source is the cell's full-area rear side metallization. We hence propose the use of a SiN_x layer as rear side mirror to reduce the parasitic absorption to 11.7%. This change can lead to a 3.2 °C lower module operating temperature, which results in an about 5 W higher electrical power output when considering a typical 260 W module.

Peer review by the scientific conference committee of SiliconPV 2015 under responsibility of PSE AG

Keywords: Ray tracing; thermal solar module behaviour; simlation; dielectric rear side mirror; solar module temperature;field measurements.

* Corresponding author. Tel.: +49-511-762-17253.
E-mail address: vogt@solar.uni-hannover.de

Peer review by the scientific conference committee of SiliconPV 2015 under responsibility of PSE AG
doi:10.1016/j.egypro.2015.07.030

1. Introduction

We look at benefits and possibilities to include thermal properties in the numerical modelling of the electrical properties of c-Si solar cells embedded in the module. The performance and yearly yield of a module does not only depend on the temperature coefficient of the c-Si solar cells, but also on the thermal properties of the module itself, i.e., by how much the cell's temperature is raised above the ambient temperature. This temperature difference depends most strongly on wind speed (considered for a given solar irradiation flux), and to a smaller extent on the thermal properties of the module, such as heat conduction and emissivity. In this work, we establish a coupled semiconductor/thermal model, validate it with measurements and field data from a solar module in an outdoor test, and show potential for improvement.

Nomenclature

ε	Dielectric function	Q	Heat source
Ψ	Electric potential	k	Thermal conductivity
q	Charge	C_p	Heat capacity
p	Hole density	ρ	Material density
n	Electron density	P	Power
N_{acc}^{-}	Acceptor density	ε_{sur}	Surface emissivity
N_{don}^{+}	Donator density	σ	Stefan Boltzmann constant
t	Time	T	Temperature
$\vec{J}_n$	Electron current density	$\vec{n}$	Normal to the module surface
$\vec{J}_p$	Hole current density	h	Heat transfer coefficient
G	Generation rate	v_{wind}	Wind speed
R	Recombination rate	L	Module length
μ_n	Electron mobility	μ_{vis}	Air's viscosity
μ_p	Hole mobility	R_{al}	Raleigh number
D_n	Electron diffusion	φ	Module tilt angle
D_p	Hole diffusion		

2. Simulation model

Nowadays, excellent software is available for multiphysics simulations, such as the finite-element method (FEM) software COMSOL . In a first step, we implemented into COMSOL the same semiconductor model for c-Si solar cells as is used in state-of-the-art SENTAURUS simulations [1]. We then coupled this model with COMSOL's equations for thermal conduction, thermal radiation, natural convection, and forced convection (by wind). This allows us to simulate the IV curves of solar cells for given irradiance, ambient temperature and wind speed, while keeping the cell temperature floating. Fig. 1 shows the main information flow in our simulation model.

Heat sources include the parasitic absorption of sunlight throughout the module, thermalization of photo-generated carriers in Si, their recombination, and entropy generation during charge carrier extraction. The parasitic absorption and photo-generation are calculated with sophisticated ray tracing [2]. This allows us to investigate the effects of parasitic absorption on the module temperature more accurately than most previous works on thermal PV module behavior such as [3, 4], where the optical properties were averaged over all wavelengths.

As shown in the schematic of Fig. 1, we then use the circuit simulation tool LTSPICE IV to calculate module power from the cell's IV curves.

2.1. Semiconductor and cell properties

We implemented a well established semiconductor model for c-Si solar cells [1] into the recently developed semiconductor module of COMSOL. We solve the semiconductor (Poisson (1), continuity (2), (3) and transport (4),

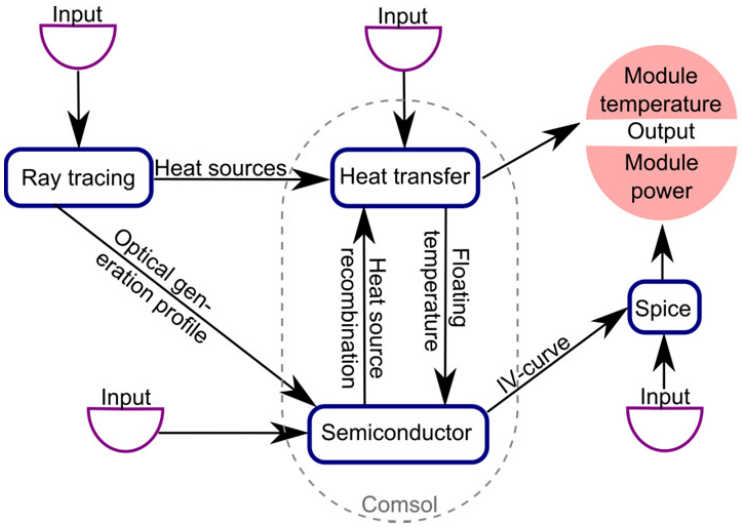

Fig. 1. Schematic of the simulation model showing the information flow between the different simulations.

(5)) equations listed here with the temperature kept floating and coupled to the module's thermal simulation:

$$\nabla(\varepsilon \cdot \nabla\Psi) = -q\left(p - n + N_{don}^{+} - N_{acc}^{-}\right) \tag{1}$$

$$\frac{\partial n}{\partial t} = \frac{1}{q}\nabla\vec{J}_n + G - R \tag{2}$$

$$\frac{\partial p}{\partial t} = -\frac{1}{q}\nabla\vec{J}_p + G - R \tag{3}$$

$$\vec{J}_n = -q\mu_n n\nabla\Psi + qD_n\nabla n \tag{4}$$

$$\vec{J}_p = -q\mu_p p\nabla\Psi - qD_p\nabla p\,, \tag{5}$$

where the symbols have their usual, well-known meaning shown in the Nomenclature. An industrial standard c-Si solar cell with an efficiency of 18.5% at an operating temperature of 25°C is taken as an example. With free-carrier mobility, band gap narrowing, Auger recombination, and radiative recombination all being implemented in a temperature dependent manner [1], the cell's temperature coefficient turns out to be $0.5\%_{rel}/°C$, which is in good agreement with literature [5].

2.2. Heat transfer and module properties

The three equations for the thermal conduction (6), radiation (7) and convection (8) used in the model are as follows:

$$\rho \cdot C_p \cdot \frac{\partial T}{\partial t} = \nabla \cdot (k \cdot \nabla T) + Q \tag{6}$$

$$P = \varepsilon_{sur} \cdot \sigma \left(T_{amb}^4 - T^4 \right) \tag{7}$$

$$-\vec{n} \cdot (-k \cdot \nabla T) = h \cdot \left(T_{amb} - T \right). \tag{8}$$

Again the symbols' meaning can be found in the Nomenclature. These equations are solved in a fully coupled manner with the semiconductor model, from where heat due to thermalization, recombination, and charge carrier extraction is taken. While the ray tracing is done in full-size 3D, the semiconductor/thermal part can be reduced to one dimension with only little error which allows for very fast computation times. The one dimensional model is symbolized by the red line in Fig. 2, it consists six of layers with different thermal properties from top to bottom: glass, encapsulant, cell, cell rear reflector, encapsulant and back sheet (see section 2.3 for further details on the simulated module). The time to reach a fully-coupled solution of this one dimensional semiconductor/thermal model implemented in COMSOL is about 3 minutes on a typical desktop computer (4 CPUs, 3 GHz, 8 GB RAM).

Each layer has its own heat source Q, which is calculated via ray tracing except for the cell since there is an additional heat source due to recombination. For the thermal radiation equation (7), we assumed the ground below the module to have ambient temperature, and we calculated the sky's temperature via an approximation from [6].

The thermal convection equation describing the interaction with the air above and below the module is very dependent on the assumed heat transfer coefficient h between module and air. For the module's front side, we assumed forced convection (9) to calculate the heat transfer coefficient h, dependent on wind speed. For both the front and the back side, we assume natural convection (10) of a tilted plate to calculate the thermal convection between the air and the module surface independent of wind speed.

The heat transfer coefficient in the case of forced convection (dependent on wind) was derived from:

$$h_{froced} = 2 \frac{k \cdot 0.3387 \cdot \left(\mu_{vis} \cdot C_p / k \right)^{1/3}}{L \left(1 + \left(0.0468 \cdot k / \mu_{vis} \cdot C_p \right)^{2/3} \right)} \cdot \sqrt{\rho \cdot v_{wind} \cdot L / \mu_{vis}}. \tag{9}$$

And in the case of natural convection (independent of wind):

$$h_{natural} = \frac{k}{L} \left(0.68 + \frac{0.67 \cdot \sqrt[4]{\cos(\varphi) \cdot R_{al}}}{\left(1 + \left(0.492 \cdot k / \mu_{vis} C_p \right)^{9/16} \right)^{4/9}} \right). \tag{10}$$

As always the symbols' meaning can be found in the Nomenclature. The φ is the module tilt angle is measured versus a vertical wall more details on the heat transfer coefficient between air and a solid plate can be found in [7, 8].

2.3. Calculation of heat sources using ray tracing

The ray tracing is done in three dimensions. The ray tracing framework DAIDALOS [2] with a multi-domain-approach [9] is used. This allows us to simulate entire 60 cell solar module, while also taking into account the front metallization and the more than 10^{10} pyramids of the texture.

The module we ray trace is shown in Fig. 2. It consists of a 3.2 mm thick float glass with an anti reflection coating (ARC) on top, 450 µm encapsulant above and below the cell, the modules rear side is covered by a white back sheet. The distance between two cells is 3 mm and the distance to the frame is 10 mm. The cell has a front side metallization, SiN_x ARC layer, random pyramids as texture, a pseudo squared shape of a 15.6·15.6 cm² wafer with 180 µm thickness and full area rear side reflector with 350 µm thickness.

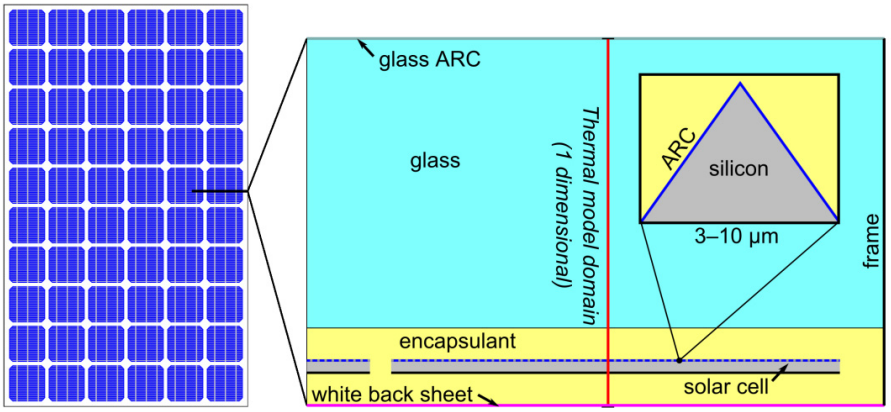

Fig. 2. Schematic of the simulated solar cell module. The ray tracing includes the whole module in 3 dimensions, while the thermal simulation model is in 1 dimension indicated by the red line.

As a light source, we assume vertical incidence of the standard AM1.5G spectrum in the wavelength range between 300 and 2500 nm and simulate 10 000 rays every 10 nm. The time for one ray tracing simulation as described is about 20 minutes on a typical desktop computer (4 CPUs, 3 GHz, 8 GB RAM), about 75% of the simulation time is spend on rays above 1200 nm since they typically travel much further within the module.

2.4. Calculation of module power with spice

Because the cells are connected in series in a standard 60 cell module, we simulate the module power with the circuit simulator LTSPICE IV from Linear Technology, considering all interconnector resistances. All cells gain a part of their J_{sc} from light, which is reflected by the back sheet before it hits the cell. However, cells located next to the frame have 10 mm of back sheet next to them on at least one side, thus they have a higher J_{sc} than middle cells with just 3 m back sheet on every side. Hence we adjust the cells' J_{sc} values according to their position in the module: our ray tracing analysis shows that the cells on the edge of the module add a factor of 1.0126 to each J_{sc} and 1.026 in case of a corner cell. Due to the series interconnection of the cells, however, only part of these current-gains are exploited by the module.

3. Heat sources

The standard AM1.5G spectrum [10] normalized to 1000 W/m² between 250-4000 nm has 99% of it's irradiance between 300-2500 nm. Therefore we can concentrate on the wavelength range between 300-2500 nm and ignore other wavelengths with little error. As shown in Fig. 3, about 20% of the irradiance is in the infrared (IR), where even a cell operating at the Lambertian limit cannot absorb it.

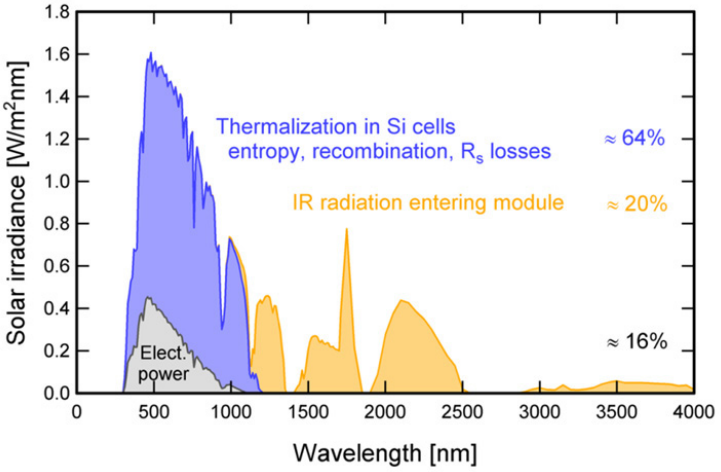

Fig. 3. AM1.5G spectrum compared to a cells electrical power output when operating at 16%.

In addition to the IR losses, there are also thermalization, recombination, resistance and entropy losses in each cell to consider. The last two are only being considered when calculating the cells *IV* curves and the modules power, but their impact as heat sources is not included yet. In table 1, a comparison of parasitic absorption and thermalization losses of each module type for different wavelength ranges is shown. Here we consider three module types:

- EVA encapsulant and full-area rear side aluminum metallization.
- Silicone encapsulant and full-area rear side aluminum metallization.
- EVA encapsulant and full area SiN_x dielectric rear side mirror.

Because the cell's ARC and the front side metallization are not explicitly included in the one dimensional COMSOL model, their parasitic absorption is added to the cell's heat source (HS). Hence, the IR absorbance of the front metallization causes the cells to have a heat source in the IR. Considering the standard module, about 18.9% of the sun's intensity becomes parasitically absorbed. Replacing the full-area rear side metallization with an SiN_x dielectric mirror lowers the parasitic absorbance to 11.7%. The SiN_x has an refractive index of n=2.09 at 633nm and a thickness of 100 nm. It replaces the full aluminum contact of the standard cells. The aluminum absorbs about 10% of the sun's intensity, mostly in the IR. The dielectric mirror improves that drastically and causes higher reflection.

Table 1. Comparison of heat sources (HS) via parasitic absorption and thermalization of each module type considered here, for the complete spectrum in the wavelength range between 300-2500 nm and the wavelength range between 1200-2500 nm, where silicon is nearly transparent.

Module Type (Encapsulant + cell rear side mirror)	Wavelength range [nm]	HS cell [W/m²]	HS glass [W/m²]	HS encapsulant [W/m²]	HS rear side mirror [W/m²]	HS back sheet [W/m²]	Reflected [W/m²]
EVA + Al	300-2500	265.4	38.3	43.2	101.8	6.1	148.1
EVA + Al	Above 1200	2.1	14.2	3.2	73.3	3.2	58.3
Sil + Al	300-2500	280.3	35.6	5	104.6	8.1	164.5
Sil + Al	Above 1200	1.9	12	2	75	2.7	60.5
EVA + SiN_x	300-2500	266.2	47.5	47.3	0	20.6	217.1
EVA + SiN_x	Above 1200	2.5	17.3	5.8	0	16.8	111.8

Switching from an EVA encapsulated module to a silicone encapsulated module also lowers the parasitic absorbance to 15.3%, however most of that improvement is not in the IR and therefore it was already noticed, when no thermal properties were considered [11, 12]. This improvement is also visible by the increase in the cells heat source by 5.6% for the silicone encapsulated module, due to higher thermalization losses.

4. Field measurements

The module performance, the irradiance on the module, module and ambient temperatures, and wind speed were collected in an outdoor testing facility near Cologne in Germany by TÜV-Rheinland from 1. August 2011 until 31. August 2012. Measurements were made every 30 seconds in daylight.

In the following, we filter the measured data for an interval of ±1.5 °C around the investigated ambient temperature and an interval of ±15 W/m² for each radiation level to have a sufficient number of data points. The data for an ambient temperature of 25 °C is shown in Fig 4. It illustrates the correlation between module (backside) temperature, wind speed and the impinging irradiance. As expected, the module temperature increases with more incoming radiation and decreases with increasing wind speed.

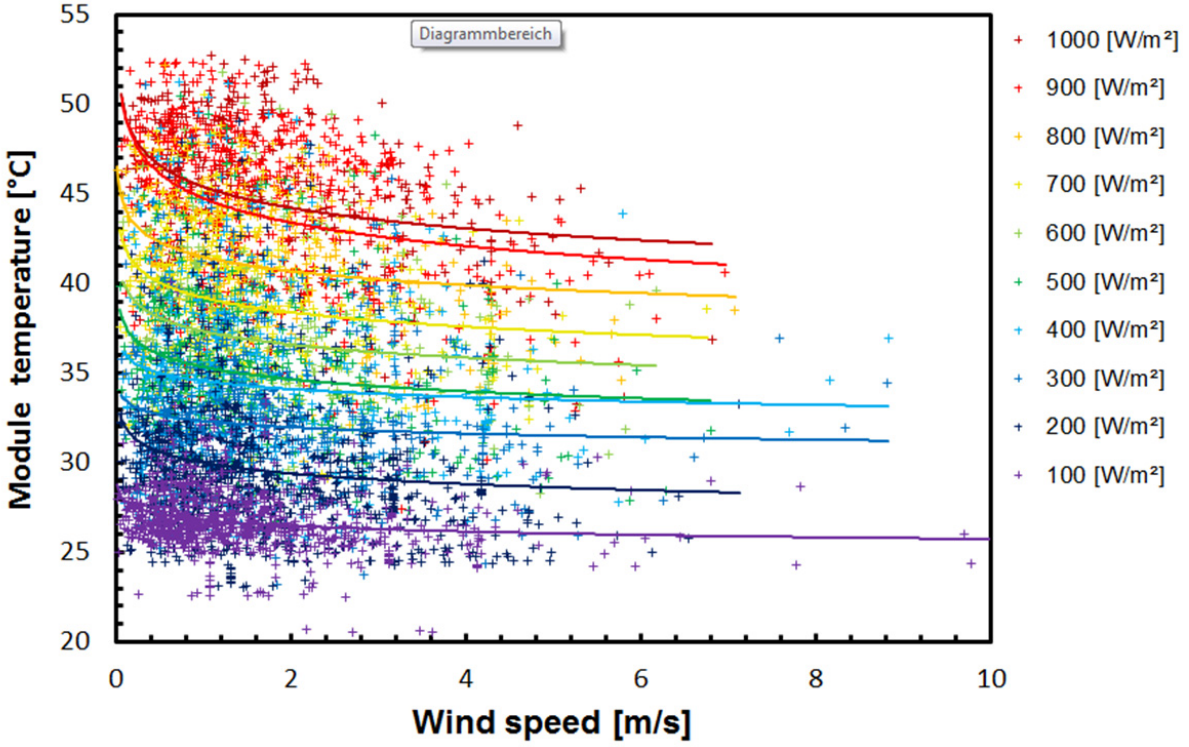

Fig. 4. Symbols: Measured module (backside) temperature and wind speed at the indicated impinging irradiance (in the range of ±15 W/m^2), at an ambient temperature of (25 ±1.5) °C. The lines are least-square power-fits.

Fig. 5 shows the distribution of wind speed at daylight during the monitored period of one year. Our analysis showed that this distribution varies only weakly with irradiance, therefore, only the total data is shows here. At the site near Cologne, the wind speed is mainly below 4 m/s and hardly ever exceeds 8 m/s. Note that in Fig. 4, the largest temperature variation occurs in the slow wind range from 0 to 3 m/s, which prevails in 65% of the daytime at the site near Cologne. At higher wind speeds than 3 m/s, only modest additional temperature reductions occur. Thus, one should optimize these solar modules for slow wind conditions.

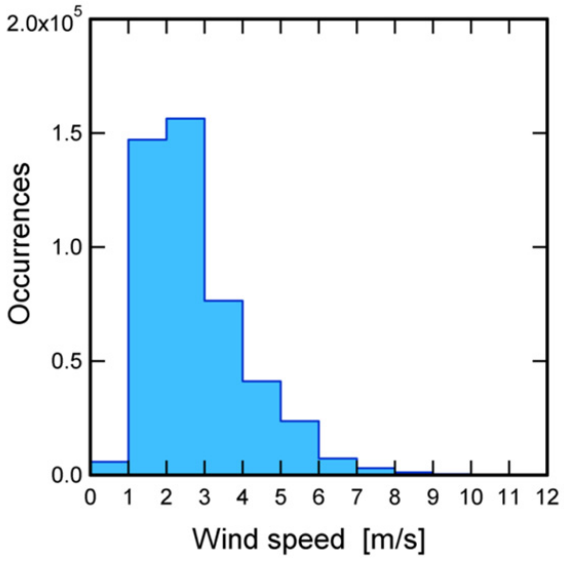

Fig. 5. Histogram of wind speed at daylight over one year at the site near Cologne, Germany.

4.1. Model validation via field measurements

In the following, we validate our thermal simulation model by comparing it to the field measurements. For the heat sources in our simulation, we selected the standard module in the top row from table 1 and scaled the intensity of the incoming radiation.

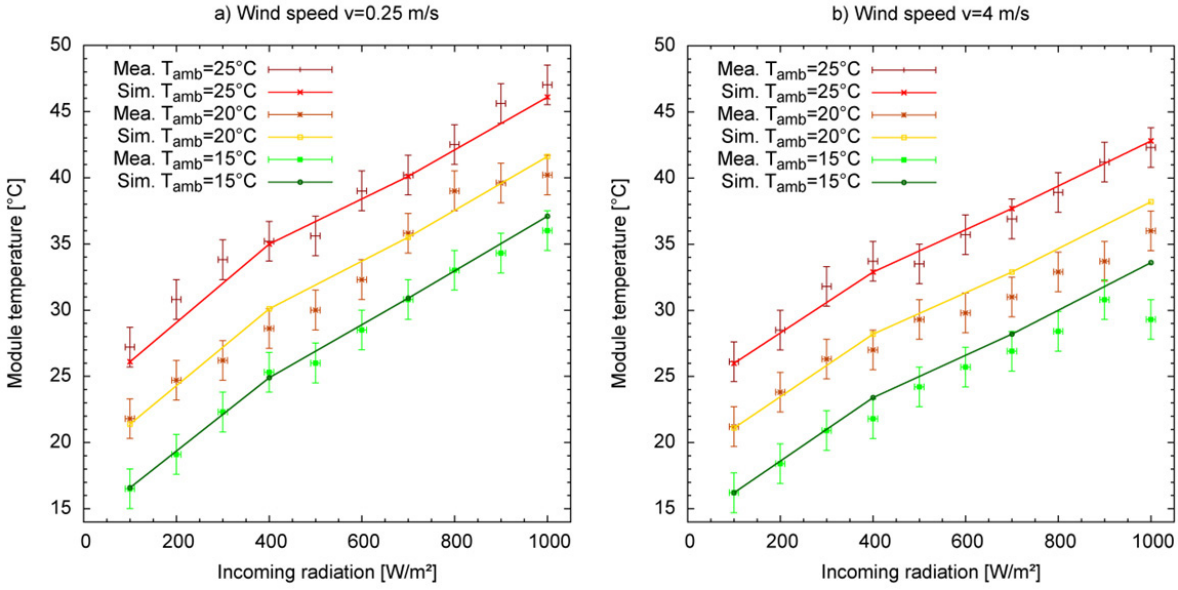

Fig. 6. Comparison of simulated (lines) with measured (symbols) module temperature for different ambient temperatures and radiation levels. The error bars indicate the standard deviation of the measurement points from Fig. 4. (a) Shows the case for a wind speed of (0.25 ± 0.25) m/s, (b) of (4 ± 0.5) m/s.

Both graphs in Fig. 6 show the module backside temperature versus the incoming radiation for three different ambient temperatures: 15, 20 and 25 °C. The simulations and the measurements show a nearly linear increase of module temperature with radiation for each given ambient temperature and wind speed. The average measured temperature increases by about (2 ±0.8) °C per 100 W/m² irradiance, the simulated temperature by (2.2 ±0.5) °C, which is within the standard deviation of the measurements (shown as error bars). Looking at the data more closely, one can see that the bigger $\Delta T=T_{mod} - T_{amb}$ the lower the temperature increase for the next 100 W/m² of more in radiation.

Considering the results for 0.25 m/s wind speed, there is very good agreement. For the 4 m/s scenario and for ambient temperatures of 15 °C and 20 °C, the simulations project a slightly higher module temperature than the field measurements. However, in the case with 25 °C ambient temperature the agreement is quite good. It has been reported by Armstrong [3] that the Nussuelt Relation which we use the calculate the heat transfer coefficient h for forced convection (9), is to low. However, Armstrong also discusses ten other formulas for calculating the impact of wind speed on the solar module. After comparing all of them, we discovered that this forced convection formula (9) leads to the biggest agreement between our simulations and the field measurement.

5. Results and discussion

Table 2 lists the simulated results of four different modules at 25 °C ambient temperature, with an impinging irradiance of 1000 W/m², the AM 1.5G spectrum, and 0 m/s wind speed. We choose the same optical generation profile within the cells for all module types in order to clarify the impact of different thermal behaviors. Meaning that if each module would be operating at the ambient temperature of 25 °C, the cells efficiencies would be 18.5% and each module would have an electrical power output of 262 W.

The module in the top row represents a standard module with EVA encapsulant and full-area Al back contact. At the assumed conditions, our simulation predicts that it's back side temperature is 46.5 °C and that it generates 12% less electrical power than it would if it operated at ambient temperature. The module with silicone encapuslant instead of EVA operates at a about 0.9 °C lower temperature due to the lower parasitic absorption in the silicone which leads to the higher reflection from all module components below the silicone.

Replacing the full-area back side metallization with an full area dielectric mirror leads to more than 3.2 °C cooler operating temperature since it lowers the parasitic absorption from 18.9% to 11.7%. Covering the entire module with a 100% reflector for light between 1205-2500 nm wavelength would lead to an operating temperature 4.2 °C lower than the standard module (with EVA encapsulant and full-area Al back contact), provided the reflector doesn't change the module's thermal behavior in any other way, but blocking those wavelengths from the spectrum.

Comparing those two improvements towards a lower module operating temperature one can see that most of the improvement in thermal module behavior that can come from reducing parasitic absorption above 1200 nm is already achieved by replacing the full rear side metallization. The next biggest absorbers in the relevant IR between 1200-2500 nm are the glass and the back sheet. By reducing their absorbance to zero one could lower the solar modules operating temperature by only another 1 °C.

Table 2. Comparison of different modules operating temperatures, efficiencies and electrical power output at those temperatures for an incoming radiation of 1000 W/m² with AM 1.5G spectrum and no wind.

Module Type (Encapsulant + cell rear side mirror)	Ambient Temperature [°C]	Module Temperature [°C]	Cell efficiency [%]	Module Power [W]
EVA + Al	25	46.5	16.3	231
Sil + Al	25	45.6	16.4	232
EVA + SiN	25	43.3	16.7	236
No-IR: EVA + Al	25	42.3	16.8	237

6. Conclusion

Our simulation model reproduced the field measurements very well. Looking at the field measurements, it becomes obvious that the vast majority of the time when there is more than 100 W/m² of incoming radiation and the wind speed is below 4 m/s. Therefore it's even more important to prevent increased module operating temperatures due to parasitic absorption. Our ray tracing analysis of different solar modules under the AM.15G spectrum between 300-2500 nm shows that about 18.9% of the irradiance becomes parasitically absorbed by a standard PV module with full-area rear metallization. Replacing it with a SiN_x mirror lowers the parasitic absorbance to 11.7%, which leads to a 3.2 °C lower module operating temperature and consequently to about 5 W higher electrical power output (when considering a module with 262 W). With a conventional simulation approach, which does not take the IR radiation into account, those considerable advantages would not be noted. Therefore, it is advantageous to take also the module's thermal properties with wavelength resolution into account when optimizing solar cells and modules.

Acknowledgements

We would like to thank Markus Schweiger from TÜV Rheinland for providing us with the field measurement data.

References

[1] Altermatt PP. Models for numerical device simulations of crystalline silicon solar cells—a review. Journal of Computational Electronics 2011; 10:314-330.
[2] Holst H, Winter M, Vogt MR, Bothe K, Köntges M, Brendel R, Altermatt PP. Application of a new ray tracing framework to the analysis of extended regions in Si solar cell modules. Energy Procedia 2013; 38:86-93.
[3] Armstrong S, Hurley WG. A thermal model for photovoltaic panels under varying atmospheric conditions. Applied Thermal Engineering 2010; 30:1488-1495.
[4] Hoang P, Bourdin V, Liu Q, Caruso G, Archambault V. Coupling optical and thermal models to accurately predict PV panel electricity production. Solar Energy Materials & Solar Cells 2014; 125:325-338.
[5] Skoplaki E, Palyvos JA. On the temperature dependence of photovoltaic module electrical performance: A review of efficiency/power correlations. Solar Energy 2009, 83:614–624.
[6] Krauter S. Betriebsmodel der optischen, thermischen und elektrischen parameter von photovoltaischen Modulen. Berlin: Köster; 1993.
[7] Incropera FP and DeWitt DP. Fundamentals of Heat and Mass Transfer. 5th Ed. John Wiley & Sons, 2002.
[8] Bejan A. Heat Transfer. John Wiley & Sons, 1993.
[9] Winter M, Vogt MR, Holst H, Altermatt PP. Combining structures on different length scales in ray tracing: Analysis of optical losses in solar modules. Optical and Quantum Electronics 2014;1-7.
[10] Gueymard CA. Parameterized Transmittance Model for Direct Beam and Circumsolar Spectral Irradiance. Solar Energy 2001; 71:325-346.
[11] McIntosh KR, Cotsell JN, Cumpston JS, Norris AW, Powell NE, Ketola BM. An optical comparison of silicone and eva encapsulants for conventional silicon pv modules: A ray-tracing study. 34st IEEE Photovoltaic Specialists Conf. 2009: 544-549.
[12] Vogt MR, Holst H, Winter M, Knoc S, Ruppenthal A, Köntges M, Brendel R, Altermatt PP. Optical loss analysis of colored PV modules using comprehensive ray tracing. 2014. 6th World Conference on Photovoltaic Energy Conversion, Kyoto, Japan, 1115-1116.